

Accelerated $L_{1/2}$ Regularization Based SAR Imaging via BCR and Reduced Newton Skills

Jinshan Zeng^{1a}, Zongben Xu^{2a}, Bingchen Zhang^{3b}, Wen Hong^{4b}, Yirong Wu^{5b}

^a *School of Mathematics and Statistics, Xi'an Jiaotong University, Xi'an, 710049, China*

^b *National Key Laboratory of Science and Technology on Microwave Imaging, Institute of Electronics, Chinese Academy of Sciences, Beijing, 100190, China*

Abstract

Sparse synthetic aperture radar (SAR) imaging has been highlighted in recent studies. As an important sparsity constraint, $L_{1/2}$ regularizer has been substantiated effectively when applied to SAR imaging. However, $L_{1/2}$ -SAR imaging suffers from a common challenge with other sparse SAR imaging methods: the computational complexity is costly, especially for high dimensional applications. This challenge is mainly due to that $L_{1/2}$ -SAR imaging is a gradient descent based method, of which the convergence is at most linear. Thus, a lot of iterations are often necessary to yield a satisfactory result. In this paper, we propose an accelerated $L_{1/2}$ -SAR imaging method by applying the block coordinate relaxation (BCR) scheme combined with the reduced Newton skill for acceleration. It is numerically shown that the proposed method keeps fast convergence within a very few iterations, and also maintains high reconstruction precision. We provide a series of simulations and two real SAR applications to demonstrate the superiority of the proposed method. Particularly, much faster convergence and higher reconstruction precision in

¹Corresponding author, E-mail: jsh.zeng@gmail.com

²E-mail: zbxu@mail.xjtu.edu.cn

³bczhang@mail.ie.ac.cn

⁴whong@mail.ie.ac.cn

⁵wyr@mail.ie.ac.cn

imaging, of the proposed method over the other sparse SAR imaging methods.

Keywords: Synthetic aperture radar; $L_{1/2}$ regularization; $L_{1/2}$ -SAR imaging; block coordinate relaxation; reduced Newton acceleration.

1. Introduction

Synthetic Aperture Radar (SAR) can obtain high resolution images of illuminated scenes under all weather and day-night circumstances. It plays an important role in remote sensing, and has been widely used in many military and civilian applications, including topographic mapping, target recognition, environmental monitoring, and surveillance, etc. SAR imaging is an inverse scattering problem, more precisely, a problem of seeking for a spatial map of reflectivity from measurements of scattered electric fields, which can be normally modeled as an ill-posed linear inverse problem. For conventional SAR imaging, the high resolution of range direction is obtained by the pulse compression of transmitted signal, and the high resolution of azimuth direction is achieved through the synthetic aperture [1]. Moreover, the data acquired for the conventional SAR imaging is sampled at the Nyquist rate. According to the Shannon-Nyquist sampling theorem, the Nyquist rate is no less than two times of the signal bandwidth.

Most of traditional SAR imaging methods are based on matched filtering (MF) [2], such as Range Doppler algorithm [3], Chirp Scaling algorithm [4], etc. These algorithms can be fast implemented by the use of Fourier transformation or time-frequency interpolation. However, there are some disadvantages of these traditional MF based SAR imaging methods: First, the range and azimuth resolutions of a SAR image are directly proportional to the bandwidth of the transmitted signal and the doppler bandwidth respectively.

In order to obtain a high resolution image, therefore, a wide transmitted signal bandwidth in range and a wide synthetic doppler bandwidth in azimuth are required. Second, according to the Nyquist rate, the sampling rates in both range and azimuth must be very high for high resolution SAR imaging. This leads to much more onboard memory and downlink throughput required for the platform. Third, traditional SAR images suffer from serious sidelobe interference problem, which degenerates the quality of SAR images.

In recent years, as the fast development of compressed sensing (CS) [12, 13], sparse SAR imaging has been attracted a great deal of attention [5, 6, 7, 8, 9, 10, 11]. Compressed sensing theory suggests that it is possible to recover a sparse or compressible scene from a small number of random measurements with an appropriate nonlinear reconstruction scheme. Therefore, sparsity plays a crucial role in CS. Unlike the conventional sampling, CS is a procedure of using the sparsity of the signal and combining sampling with compression, which then permits the signal being sampled at the sub-Nyquist rate and reconstructed from the compressed measurements. Thus, the main benefit of CS applied to SAR imaging is the significant reduction of the number of necessary transmitted and/or received electromagnetic waveforms for reconstructing a high resolution SAR image. Inspired by this, many CS based algorithms have been suggested for SAR imaging.

A compressive radar imaging scheme based on CS notation was firstly reported by Baraniuk et al [6]. They employed Orthogonal Matching Pursuit (OMP) algorithm [14] for radar imaging from the compressed measurements. In [7], Alonso et al focused on the SAR raw data, and used the Regularized OMP (ROMP) algorithm [15] to implement SAR imaging. Both OMP and ROMP, are greedy pursuit algorithms, which can be quite fast, especially in the ultrasparse regime. However, they are inefficient or even failed

when the signal is not very sparse and there exists heavy observation noise [16]. In [8], a compressed SAR imaging modality was suggested based on L_1 regularization, which is a convex optimization and thus can be efficiently solved [17, 18, 19, 20]. It was also shown in [21] that, under certain conditions, the resultant solution of L_1 regularization coincide with one of the solutions of L_0 regularization (L_1/L_0 equivalence). Because of these, L_1 regularization gets its popularity and has been treated as a useful tool for solution of the sparsity problems.

In spite of its computational efficiency and well approximation of L_0 regularization, L_1 regularization cannot enforce further sparsity. L_q ($0 < q < 1$) regularization was introduced as an improvement upon performance of L_1 regularization [22, 23, 24, 25]. In particular, a new regularization framework with $L_{1/2}$ regularizer was developed by Xu et al [22, 23, 24]. Inspired by the well developed theoretical properties of $L_{1/2}$ regularization, an $L_{1/2}$ regularization based SAR imaging method ($L_{1/2}$ -SAR in briefly) was suggested in [10, 11]. It is demonstrated that $L_{1/2}$ -SAR requires much fewer measurements to reconstruct an interested scene. Also, it is more robust to noise over L_1 -SAR and the greedy pursuit based SAR imaging methods [11].

Despite its effectiveness, $L_{1/2}$ -SAR suffers from the same challenge as that for most CS based SAR imaging methods: its computational burden is heavy, especially for high dimensional SAR imaging applications. This challenge is mainly due to the fact that $L_{1/2}$ -SAR is a gradient descent based method, of which the convergence is at most linear, and thus a lot of iterations are necessary to reach a satisfactory result.

In this paper, we aim to develop an accelerated $L_{1/2}$ -SAR imaging method. The main idea is to apply the block coordinate relaxation approach for the $L_{1/2}$ -SAR imaging

procedure, and use the reduced Newton skill for acceleration (called the BCRA- $L_{1/2}$ -SAR hereafter). The block coordinate relaxation (BCR) method is widely used in minimization of a continuously differential function with multiple variables [26, 27]. A special case of BCR is the well-known (block) coordinate descent method [28], which has been extended to minimize a nondifferential (nonconvex) function with certain separability and regularity properties like continuity on a compact level set [29]. In BCR, the coordinates are partitioned into several blocks. At each iteration, the objective function descends along a relaxed descent direction with respect to one of the coordinate blocks while the other are fixed. Therefore, instead of the original high dimensional problem, a relative lower dimensional and thus commonly more easily solved problem at each iteration is solved. Thus, BCR scheme is potentially effective for high dimensional applications, especially for SAR imaging. The reduced Newton skill was previously proposed to accelerate BCR for the convex regularization problem with certain separable structure ([30]). We extend it to $L_{1/2}$ regularization, which is nonconvex.

A series of simulations and two real SAR applications are conducted to support the fast convergence and high reconstruction precision properties of BCRA- $L_{1/2}$ -SAR method. In particular, we demonstrate the outperformance of BCRA- $L_{1/2}$ -SAR over the other CS based SAR imaging methods like OMP [14] and L_1 regularization.

The reminder of the paper is organized as follows. In Section 2, we review $L_{1/2}$ -SAR method and then formulate the BCRA- $L_{1/2}$ -SAR imaging method. In section 3, we conduct a numerical study to assess the performance of BCRA- $L_{1/2}$ -SAR. In Section 4, we then provide two real SAR applications, showing the high performance and effectiveness of BCRA- $L_{1/2}$ -SAR. Finally, we conclude the paper in Section 5 with some useful remarks.

2. BCRA- $L_{1/2}$ -SAR Imaging

In this section, we first introduce the $L_{1/2}$ -SAR imaging method suggested in [11] briefly, formulate the accelerated $L_{1/2}$ -SAR imaging method, and then present some remarks of the proposed method.

2.1. $L_{1/2}$ -SAR Imaging

According to [1], the ground-plane geometry for stripmap-mode SAR is shown as in Figure 1. The radar platform travels at velocity v in the azimuth direction and transmits wideband microwave pulses at regular intervals. The corresponding echoes are recorded. Many pulses are transmitted during the so-called integration time, i.e., the time the platform takes to travel the footprint cross-range length. More specifically, a complex baseband pulse $s(\tau)$, usually Chirp, is modulated in quadrature by a carrier frequency f_0 to yield the transmitted waveform $p(\tau) = \text{Re}\{s(\tau)\exp\{j2\pi f_0\tau\}\}$, where $\text{Re}\{\cdot\}$ denotes the real part of $\{\cdot\}$. Then $p(\tau)$ is transmitted at the uniform pulse repetition interval (PRI). The received backscattered energy can be modeled as a convolution of the pulse waveform with the ground reflectivity function $f(\tau, \eta)$, where τ, η represent the fast (range) and slow (azimuth) times, respectively. Upon receiving, the echo is then quadrature demodulated to the complex baseband signal $y_r(\tau', \eta')$, that is,

$$y_r(\tau', \eta') = \iint f(\tau, \eta) g(\tau', \eta' - \eta; \tau) d\tau d\eta + e(\tau', \eta'), \quad (2.1)$$

where $g(\tau', \eta' - \eta; \tau) = \omega_\tau(\tau' - \frac{2R(\tau, \eta' - \eta)}{c}) \omega_\eta(\eta') s(\tau - \frac{2R(\tau, \eta' - \eta)}{c}) \exp\{-j4\pi f_0 R(\tau, \eta' - \eta)/c\}$, and c is the speed of light, ω_τ is the envelop function of transmitted pulse in range, ω_η is the antenna beam pattern in azimuth, $R(\tau, \eta' - \eta) = \sqrt{(c\tau/2)^2 + [v(\eta' - \eta)]^2}$ is the

slant range between radar and the target, $e(\tau', \eta')$ is assumed to be the complex white Gaussian noise arising from thermal noise in the transmitter and receiver hardware.

If one samples the continuous-time analog echo $y_r(\tau', \eta')$ with the additive complex white Gaussian noise $e(\tau', \eta')$ at the grid of time (τ'_k, η'_l) , $k = 1, \dots, K$ and $l = 1, \dots, L$, and discretizes the reflectivity field $f(\tau, \eta)$ at the grid of time (τ_i, η_j) , $i = 1, \dots, M$ and $j = 1, \dots, N$, the following SAR observation model then can be obtained

$$y = Af + e, \quad (2.2)$$

where $y \in \mathbb{C}^m$, $f \in \mathbb{C}^n$, $A \in \mathbb{C}^{m \times n}$, $e \in \mathbb{C}^m$, $m = KL$ and $n = MN$. More specifically, $y_{k+(l-1)K} = y_r(\tau'_k, \eta'_l)$, $f_{i+(j-1)M} = f(\tau_i, \eta_j)$, $e_{k+(l-1)K} = e(\tau'_k, \eta'_l)$, and $A_{(k+(l-1)K), (i+(j-1)M)} = g(\tau'_k, \eta'_l - \eta_j; \tau_i)$. The SAR imaging problem is to reconstruct the reflectivity f from the measurement (2.2).

Moreover, if reflectivity f is sparse under a basis $\Psi \in \mathbb{C}^{n \times n}$ with sparse representation x , the linear model (2.2) then can be rewritten as

$$y = Af + e = A\Psi x + e = \Phi x + e, \quad (2.3)$$

where $\Phi = A\Psi$ and $f = \Psi x$. According to [10, 11], the above inverse problem can be solved by the $L_{1/2}$ regularization scheme (the so-called $L_{1/2}$ -SAR imaging)

$$x^* = \operatorname{argmin}_{x \in \mathbb{C}^n} \{\|y - \Phi x\|_2^2 + \lambda \|x\|_{1/2}^{1/2}\}, \quad (2.4)$$

where $\|\cdot\|_{1/2}$ denotes the $L_{1/2}$ quasi-norm of \mathbb{C}^n , defined by $\|x\|_{1/2}^{1/2} = \sum_{i=1}^n \sqrt{|x_i|}$, and $\lambda > 0$ is a regularization parameter. The first term in (2.4) is a data fidelity term, which corresponds to the linear model (2.3). The second term in (2.4) incorporates the prior information on the behavior of the field f in the transformed domain Ψ , and the

nature features of the interested scene in the resulting reconstruction (say, the sparse representation x obeys the hyper-Laplace distribution).

According to [24], the solutions of problem (2.4) can be analytically expressed in a thresholding form: any solution x of the $L_{1/2}$ -SAR imaging problem (2.4) is given by

$$x = H_{\lambda\mu,1/2}(B_\mu(x)), \quad (2.5)$$

where $B_\mu(x) = x + \mu\Phi^H(y - \Phi x)$, μ is a step size, and $H_{\lambda\mu,1/2}(\cdot)$ is the complex-valued half thresholding operator defined by

$$H_{\lambda\mu,1/2}(u) = (h_{\lambda\mu,1/2}(u_1), \dots, h_{\lambda\mu,1/2}(u_n))^T, \quad (2.6)$$

for any $u = (u_1, \dots, u_n)^T \in \mathbb{C}^n$, where the complex-valued half thresholding function $h_{\lambda\mu,1/2}(\cdot)$ is defined by

$$h_{\lambda\mu,1/2}(z) = \begin{cases} \frac{2}{3}z(1 + \cos(\frac{2\pi}{3} - \frac{2}{3}\arccos(\frac{\lambda\mu}{8}(\frac{|z|}{3})^{-\frac{3}{2}}))), & |z| > \frac{\sqrt[3]{54}}{4}(\lambda\mu)^{2/3} \\ 0, & \text{otherwise} \end{cases}. \quad (2.7)$$

With the thresholding representation (2.5)-(2.7), a complex-valued iterative half thresholding algorithm for solution of the $L_{1/2}$ -SAR imaging problem (2.4) was suggested in [11], which is as follows:

$$x^{(k+1)} = H_{\lambda_k\mu_k,1/2}(B_{\mu_k}(x^{(k)})). \quad (2.8)$$

The algorithm can be seen as a procedure of Landweber iteration projected by the half thresholding operator, which is only deduced from the gradient information of the objective function. Thus, the convergence of $L_{1/2}$ -SAR is at most linear. As a result, a lot of iterations are necessary to reach a satisfactory result.

2.2. Accelerated $L_{1/2}$ -SAR Imaging

In this subsection, we formulate an accelerated $L_{1/2}$ -SAR method, called the BCRA- $L_{1/2}$ -SAR imaging method, by applying the block coordinate relaxation method and the reduced Newton skill.

First, we apply BCR to $L_{1/2}$ -SAR imaging. For this purpose, we divide x into a series of blocks without intersection, say, $\{x_{[q]}|q \in Q\}$ with $\{[q]|q \in Q\}$ being a partition of $\{1, 2, \dots, n\}$, where $Q = \{1, 2, \dots, |Q|\}$ is the index set of blocks. For any set S , we denote by $|S|$ its cardinality. It is obvious that the regularization term in (2.4), $\|x\|_{1/2}^{1/2}$, can then be split into the form:

$$\|x\|_{1/2}^{1/2} = \sum_{q \in Q} \|x_{[q]}\|_{1/2}^{1/2}. \quad (2.9)$$

Similarly, the matrix Φ can be split into the corresponding $|Q|$ blocks, $\{\Phi_{[q]}|q \in Q\}$. Thus the $L_{1/2}$ -SAR imaging problem (2.4) can be rewritten as

$$x^* = \operatorname{argmin}_{x \in \mathbb{C}^n} \left\{ \left\| y - \sum_{q \in Q} \Phi_{[q]} x_{[q]} \right\|_2^2 + \lambda \sum_{q \in Q} \|x_{[q]}\|_{1/2}^{1/2} \right\}. \quad (2.10)$$

Assume that the k -th iteration $x^{(k)}$ has been updated, and we need to yield a new update at $k+1$ -th iteration. The idea of BCR is then that $|Q|$ substeps are taken for updating. At each substep, only one coordinate block is updated while the other blocks are fixed. Specifically, to update the q -th coordinate block, one considers the subproblem

$$\min_{x_{[q]} \in \mathbb{C}^{|[q]|}} \{ \|y_q^{(k)} - \Phi_{[q]} x_{[q]}\|_2^2 + \lambda \|x_{[q]}\|_{1/2}^{1/2} \}, \quad (2.11)$$

where $y_q^{(k)} = y - \sum_{i \neq q} \Phi_{[i]} x_{[i]}^{(k)}$. From (2.8), the following relaxed iteration for solution of the subproblem is suggested

$$\hat{x}_{[q]}^{(k+1)} = H_{\lambda \mu_q, 1/2}(B_{\mu_q}(x_{[q]}^{(k)})), \quad (2.12)$$

where $B_{\mu_q}(x_{[q]}^{(k)}) = x_{[q]}^{(k)} + \mu_q \Phi_{[q]}^H(y_q^{(k)} - \Phi_{[q]}x_{[q]}^{(k)})$, μ_q is a step size, and $H_{\lambda\mu_q, 1/2}(\cdot)$ is the complex-valued half thresholding operator defined as in (2.6)-(2.7).

We observe that the gradient information is only used in (2.12), hence, it is generally not sufficient to imply fast convergence. Therefore, we further apply the reduced Newton skill to the procedure (2.12).

The reduced Newton skill was previously proposed to accelerate BCR for the following regularized optimization problem ([30])

$$\min_x \{J_\lambda(x) = f(x) + \lambda p(x)\}, \quad (2.13)$$

where f is a smooth function, p is a closed, proper, convex function with certain separable structure, and $\lambda > 0$ is a regularization parameter. The idea is to use not only the gradient information but also the second-order differential information of the objective function for defining a new descent direction on an active manifold of the current iteration. However, the reduced Newton skill cannot directly apply to the case (2.4), since in this case, $p(x) = \|x\|_{1/2}^{1/2}$, which is nonconvex. We can, however, extend the skill to such a nonconvex case, detailed as follows.

Assume that $\hat{x}_{[q]}^{(k+1)}$ is defined by (2.12) and its support set is $S_{[q]}^{(k+1)}$, that is, $S_{[q]}^{(k+1)}$ contains all the indices of non-zero components of $\hat{x}_{[q]}^{(k+1)}$. We let

$$J_{\lambda,q}(x_{[q]}) = f_q(x_{[q]}) + \lambda p_q(x_{[q]}), \quad (2.14)$$

where $f_q(x_{[q]}) = \left\| y_q^{(k)} - \Phi_{[q]}x_{[q]} \right\|_2^2$ and $p_q(x_{[q]}) = \|x_{[q]}\|_{1/2}^{1/2}$. Since $p_q(x_{[q]})$ is nondifferentiable at zero, we consider the differentiability of $J_{\lambda,q}(x_{[q]})$ on the active complex manifold,

$\mathcal{M}_{[q]}^{(k+1)} \subset \mathbb{C}^{[q]}$, of which the i -th component is defined by

$$\mathcal{M}_{[q]}^{(k+1)}(i) = \begin{cases} \mathbb{C}^1 \setminus \{0\}, & |\hat{x}_{[q]}^{(k+1)}(i)| \neq 0 \\ \{0\}, & \text{otherwise} \end{cases}, \quad \text{for } i \in [q]. \quad (2.15)$$

We then find a new iteration $x_{[q]}^{(k+1)}$ on the manifold $\mathcal{M}_{[q]}^{(k+1)}$ by using the first and second-order differential information of $J_{\lambda,q}(x_{[q]})$. To achieve this, we expand $J_{\lambda,q}(x_{[q]})$ at $\hat{x}_{[q]}^{(k+1)}$ up to the second order, to get

$$\psi_{\lambda,q}(x_{[q]}) = J_{\lambda,q}(\hat{x}_{[q]}^{(k+1)}) + \nabla f_q(\hat{x}_{[q]}^{(k+1)})^H (x_{[q]} - \hat{x}_{[q]}^{(k+1)}) + \frac{1}{2} (x_{[q]} - \hat{x}_{[q]}^{(k+1)})^H \nabla^2 f_q(\hat{x}_{[q]}^{(k+1)}) (x_{[q]} - \hat{x}_{[q]}^{(k+1)}), \quad (2.16)$$

Then we take the new update $x_{[q]}^{(k+1)}$ as the minimizer of $\psi_{\lambda,q}(x_{[q]})$ on $\mathcal{M}_{[q]}^{(k+1)}$:

$$x_{[q]}^{(k+1)} = \arg \min_{x_{[q]} \in \mathcal{M}_{[q]}^{(k+1)}} \psi_{\lambda,q}(x_{[q]}). \quad (2.17)$$

Since (2.17) is a constrained optimization problem, it is generally difficult to solve directly.

We then propose to transform it into an unconstrained optimization problem, detailed as follows.

Denote by $P_{[q]}$ the matrix whose columns are those of the $[q] \times [q]$ identity matrix, $I_{[q]}$, corresponding to $S_{[q]}^{(k+1)}$ (i.e., $P_{[q]} = I_{[q]}|_{S_{[q]}^{(k+1)}}$). Then for any $x_{[q]} \in \mathcal{M}_{[q]}^{(k+1)}$, there exists a unique $x_s \in \mathbb{C}^{|S_{[q]}^{(k+1)}|}$ such that $x_{[q]} = P_{[q]}x_s$ (particularly, x_s can be taken as $P_{[q]}^H x_{[q]}$). We remodel problem (2.17) as the following unconstrained optimization problem

$$x_s^{(k+1)} = \arg \min_{x_s \in \mathbb{C}^{|S_{[q]}^{(k+1)}|}} \left\{ \nabla f_q(\hat{x}_{[q]}^{(k+1)})^H P_{[q]} d_s^{(k+1)} + \frac{1}{2} d_s^{(k+1)H} P_{[q]}^H \nabla^2 f_q(\hat{x}_{[q]}^{(k+1)}) P_{[q]} d_s^{(k+1)} \right\}, \quad (2.18)$$

with $d_s^{(k+1)} = x_s - \hat{x}_s^{(k+1)}$ and $\hat{x}_s^{(k+1)} = P_{[q]}^H \hat{x}_{[q]}^{(k+1)}$. Actually, after some simplifications,

problem (2.18) is equivalent to the following least square problem

$$x_s^{(k+1)} = \arg \min_{x_s \in \mathbb{C}^{|S_{[q]}^{(k+1)}|}} \{ \|y_q^{(k)} - \Phi_{S,q} x_s\|_2^2 \}.$$

Thus, the new iteration $x_{[q]}^{(k+1)}$ can be specified as

$$x_{[q]}^{(k+1)} = P_{[q]} x_s^{(k+1)}. \quad (2.19)$$

To summarize, the BCRA- $L_{1/2}$ algorithm we proposed can be summarized as Algorithm 1.

2.3. Some Remarks

(i) *Algorithm Illustration.* As shown in Algorithm 1, the BCRA- $L_{1/2}$ algorithm can be operated as the following procedure: (1) block partition: partitioning the coordinates and the corresponding sensing matrix into several blocks; (2) updating the regularization parameter; (3) inner loop iteration: for each block coordinates, (i) taking iterative half thresholding scheme to obtain a signal proxy, (ii) identify the support set of the obtained signal proxy, (iii) updating the coefficients of the identified support set via least square principle; (4) termination test. It is seen that in BCRA- $L_{1/2}$ algorithm, the crucial factors for affecting its performance includes block partition scheme, regularization parameter setting, updating rule for iteration. Among these, the block partition scheme and regularization parameter setting will be discussed in the later remarks. It is well known that the support set takes a key role in the sparsity problems. Once the support set is determined, the coefficients can be obtained by various methods directly. According to [22, 24], $L_{1/2}$ regularization can be accepted as a good variable selector. In our case, it can not only select the correct support set adaptively, but also yield the corresponding update

values. However, it is well known that there are amplitude bias problems for the simple CS estimators like L_1 and $L_{1/2}$ regularization, that is, they will slightly, yet systematically, underestimate the amplitudes of the coefficients. To overcome this, we have taken the least square rule to modify the coefficients, which will bring higher reconstruction precision in imaging as demonstrated by the latter simulations.

(ii) *On Block Partition.* It is obvious that the performance of the proposed BCRA- $L_{1/2}$ algorithm hinges upon the specific choice of block partition scheme, since the choice determines the complexity and extent of speed-up of the algorithm. In principle, the coordinate block can be partitioned in any manner, say, in any stochastic or deterministic ways. Generally, we prefer the deterministic way for convenience of implementation and analysis. Moreover, if the orthogonality information among the columns of the sensing matrix is known, we can suggest a delicate block partition scheme based on an interesting observation on the solution of subproblem (2.11), which will be further analyzed in the following. Otherwise, we prefer the sequential block partition scheme for simplicity, that is, the coordinates are partitioned sequentially into several blocks with fixed size.

Let us suppose that the submatrix $\Phi_{[q]}$ corresponding to the q -th block satisfies the following unitary condition, that is,

$$\Phi_{[q]}^H \Phi_{[q]} = \nu_q I_{|[q]|}, \quad (2.20)$$

where $\nu_q > 0$ is any positive real number. Then, we can observe that through choosing $\mu_q = 1/\nu_q$ in the thresholding representation formula (2.5)-(2.7), the solution of subproblem (2.11) can be explicitly represented as the following closed form:

$$\hat{x}_{[q]}^{(k+1)} = H_{\lambda\mu_q, 1/2}(\mu_q \Phi_{[q]}^H y_q^{(k)}). \quad (2.21)$$

Consequently, the new update (2.19) can be analytically expressed as

$$x_{[q]}^{(k+1)} = \mu_q P_{[q]} P_{[q]}^H \Phi_{[q]}^H y_q^{(k)}. \quad (2.22)$$

This observation shows that as long as a block partition scheme is made to satisfy the unitary condition (2.20), the BCRA- $L_{1/2}$ algorithm can be of a very simple form, and therefore can be most efficiently implemented. Thus, in this case, we suggest the use of the scheme of block partition to satisfy (2.20).

With the unitary partition scheme, the whole update procedure of all the blocks can be uniformly expressed, say, as follows

$$\hat{x}^{(k+1)} = H_{\lambda^{(k)}\alpha, 1/2}(x^{(k)} + \text{diag}(\alpha)\Phi^H(y - \Phi x^{(k)})), \quad (2.23)$$

and

$$x^{(k+1)} = \text{diag}(S^{(k+1)})(x^{(k)} + \text{diag}(\alpha)\Phi^H(y - \Phi x^{(k)})), \quad (2.24)$$

where, for any $z = (z_1, z_2, \dots, z_n)^T \in \mathbb{C}^n$, $\text{diag}(z) = \text{diag}\{z_1, z_2, \dots, z_n\}$, $\alpha \in \mathbb{R}_+^n$ with $\alpha(i) = \mu_q$ if $i \in [q]$ for $q = 1, 2, \dots, |Q|$, $H_{\lambda^{(k)}\alpha, 1/2}$ is the half thresholding operator with the parameters $\lambda^{(k)}$ and α , that is,

$$H_{\lambda^{(k)}\alpha, 1/2}(x) = (h_{\lambda^{(k)}\alpha(1), 1/2}(x_1), \dots, h_{\lambda^{(k)}\alpha(n), 1/2}(x_n))^T, \quad (2.25)$$

$h_{\lambda^{(k)}\alpha(i), 1/2}$ is defined by (2.7), and $S^{(k+1)}$ is the indicator vector of the support set of $\hat{x}^{(k+1)}$, i.e., $S^{(k+1)}(i) = 1$ if $i \in \text{supp}\{\hat{x}^{(k+1)}\}$ and $S^{(k+1)}(i) = 0$ otherwise.

It is observed that, with the unitary block partition scheme, the proposed BCRA- $L_{1/2}$ algorithm degenerates actually to a two-stage iterative thresholding algorithm with the well-known block coordinate descent [29] for $L_{1/2}$ regularization in the first stage and a modification via the reduced Newton acceleration skill in the second stage.

(iii) *On Regularization Parameter Setting.* Besides the block partition scheme, another factor of BCRA- $L_{1/2}$ algorithm is the regularization parameter setting. Cross-validation [31] and generalized cross-validation [32] are considered as the most commonly used methods. However, these are time-consuming, especially for high dimensional problems. Alternatively, some heuristic approaches have been suggested in [24, 33]. The basic ideal of those approaches is to treat the regularization algorithm as a tuning parameter problem whose values are determined according to the sparsity level (i.e., the number of the nonzero components of the unknown sparse signal). We follow this latter approach. More specifically, if x^* is a solution of the problem (2.4) with s -sparsity, we let

$$B_\alpha(x^*) = x^* + \text{diag}(\alpha)\Phi^H(y - \Phi x^*), \quad (2.26)$$

and

$$\Lambda(x^*) = \frac{\sqrt{96}}{9} \text{diag}(\alpha)^{-1} |B_\alpha(x^*)|^{3/2}. \quad (2.27)$$

Then it can be justified that the optimal regularization parameter λ^* satisfies

$$\lambda^* \in [[\Lambda(x^*)]_{s+1}, [\Lambda(x^*)]_s], \quad (2.28)$$

where $[\Lambda(x^*)]_s$ represents the s -th largest component of $\Lambda(x^*)$. Thus, as shown in [24], a nearly optimal regularization parameter setting strategy in implementation of the BCRA- $L_{1/2}$ algorithm can be given by

$$\lambda^{(k)} = [\Lambda(x^{(k)})]_{s+1}, \quad (2.29)$$

where $\{x^{(k)}\}$ is any approximation sequence of x^* .

It is observed that the suggested strategy depends on the prespecified sparsity level s of the unknown signal. Therefore, the estimation of sparsity level s is critical. In

applications, we may conduct an empirical study or based on some known prior to yield a reasonable approximation of s .

(iv) *On Computational Complexity.* The computational complexity of BCR- $L_{1/2}$ algorithm in each iteration step can be analysed as follows. The block partition can be done off-line. Let us consider the general block partition case. As shown in Algorithm 1, the total computational complexity of $\Phi_{[q]}x_{[q]}^{(k)}$ for $q = 1, 2, \dots, |Q|$ is $O(mn)$ at $k + 1$ -th iteration. At the inner loop, for q -th block coordinates, the computational complexity of updating $\hat{x}_{[q]}^{(k+1)}$ is $O(m|[q]|)$, and the computational complexity of modifying the q -th block coordinates $x_{[q]}^{(k+1)}$ can be neglected since $|S_q^{(k+1)}| \ll m$ generally. Consequently, the total computational complexity of the inner loop is $O(mn)$ since $\sum_{q=1}^{|Q|} |[q]| = n$. Hence, the computational complexity per iteration of the algorithm is $O(mn)$, which is the same order with that of the $L_{1/2}$ -SAR imaging method shown as in (2.8).

We will show in the next section that the number of iterations required by the proposed algorithm is significantly fewer than those required by other reconstruction algorithms.

3. Simulations

In this section, some fundamental properties of BCRA- $L_{1/2}$ -SAR imaging method, including the fast convergence speed and high reconstruction precision are verified by a series of one-dimensional (1-D) simulations. Moreover, the phase transition diagrams are presented to show the sparse reconstruction ability of the proposed method. The advantages of the new method are demonstrated by comparing it with $L_{1/2}$ -SAR imaging method [11], the L_1 and orthogonal matching pursuit algorithm (OMP) [14] based SAR imaging methods (called, L_1 -SAR and OMP-SAR for short). In simulations, we employed the

fast iterative shrinkage-thresholding algorithm (FISTA) [18] for L_1 regularization. This is adequate since it is known that FISTA is an essential L_1 regularization algorithm which is efficient for high-dimensional problems (this is crucial for SAR imaging application). In all experiments, the terminational criterions of all the employed algorithms except OMP were taken as: $\|x^{(k+1)} - x^{(k)}\|_2 / \|x^{(k+1)}\| < 10^{-6}$. The termination criteria of OMP was taken as the maximum iteration number at which the sparsity level can be attained. Moreover, the block partition and some parameters of the proposed method were set as follows: the coordinates were partitioned empirically into three blocks with the same size, and the regularization parameter was set according to (2.29).

All the experiments were implemented in a personal computer (2.51GHz, 127GB of RAM, Quad-Core AMD Opteron(tm) Processor 8380) with MATLAB 7.12.0 platform (R2011a).

The simulations were implemented in the subsequent way. First, the round-trip delay for a collection of point targets was randomly generated from a uniform distribution corresponding to a range of valid distances. Then, the complex scattering coefficient of each target was randomly assigned from a Rayleigh distribution in amplitude and a uniform distribution in phase. Finally, the received signal was generated as the sum of the time-shifted replicas of the transmitted waveform (which was adjusted to be a chirp signal), with each being multiplied by its corresponding scattering coefficient. The aim of the simulations was to recover the scattering coefficients from the echo by the related algorithms.

3.1. Convergence of BCRA- $L_{1/2}$ Algorithm

In order to evaluate the convergence of BCRA- $L_{1/2}$ algorithm, we conducted a group of 1-D simulations described as above with different experiment parameters (s, m, n) , where s is the sparsity level of the scattering coefficients, m is the measurement number and n is the dimension of the scattering coefficients. In the simulations, the experiment parameters were set as $s = 200$, $n = 10000$, and m varied from 2000 to 10000 with the same interval 2000.

The simulation results are depicted in Figure 2. In Fig. 2, the horizontal axis represents the number of iterations, and the vertical axis represents the iteration error in the logarithmic scale with 10 as the base, defined by $\lg \frac{\|x^{(k)} - x^*\|_2}{\|x^*\|_2}$, where $x^{(k)}$ is the k -th iteration, and x^* is the ground-truth scattering coefficients. The red line with circle, green line with x-mark, blue line with plus, cyan line with star, and black line with square represent the iteration results of $m = 2000, 4000, 6000, 8000, 10000$, respectively. It can be seen from Figure 2 that the BCRA- $L_{1/2}$ algorithm converges very fast. In all cases, a very few iterations (averaging 8 iterations) are sufficient for convergence of the new method. Moreover, under the same setting of the scattering coefficients, the more measurements are used, the fewer iterations are necessary for convergence in general. It is mainly due to the fact that the ill-posedness of the SAR imaging problem commonly gets better when more measurements used.

3.2. Outperformance of BCRA- $L_{1/2}$ Algorithm

The outperformance of BCRA- $L_{1/2}$ algorithm over other sparse SAR imaging methods was demonstrated in this subsection.

We have conducted a series of experiments with different parameter triplets (s, m, n) , where $s = 200$, $m = 2000$, and n varied from 2000 to 20000 with the same interval 2000. For each setting, the recovery precision, running time and iteration number were recorded. The recovery precision was evaluated by relative mean square error (RMSE), defined by $\text{RMSE} = \|x - x^*\|_2 / \|x^*\|_2$, where x and x^* represent the recovery and the ground-truth signal, respectively. The corresponding experiment results are shown in Figure 3.

As shown in Figure 3 (a) and (b), among all the tested algorithms, the recovery accuracy of the new method is the best. More specifically, the recovery accuracy of the new method is with the order of 10^{-15} , which is slightly better than those of OMP-SAR method. While the recovery accuracies of $L_{1/2}$ -SAR and L_1 -SAR methods are worse with the order of 10^{-5} . As an additional surprise, high reconstruction precision of the new method is mainly due to the fact that the amplitude bias problems of simple CS estimators like L_1 and $L_{1/2}$ regularization may be overcome via taking the least square principle to refine the coefficients. Furthermore, the recovery error of the new method keeps stable with slight oscillation, while that of $L_{1/2}$ -SAR method increases fast as the signal dimension increases. Also, the new method is the fastest when the signal dimension is more than 10^4 , as compared to the other algorithms, as shown in Figure 3 (c). In terms of the tendency of running time as the dimension increases, the new method increases much slower than the other algorithms, as shown in Figure 3 (d). In the case of $n = 20000$, the running time of the new method is 87.23 seconds, while $L_{1/2}$ -SAR, L_1 -SAR and OMP-SAR methods take 189.8, 268.3 and 732.6 seconds, respectively. The running time of $L_{1/2}$ -SAR, L_1 -SAR and OMP-SAR methods are more than 2, 3 and 8 times that of the new method, respectively. Moreover, as indicated in Figure 3 (e) and (f), the iteration

number of the new method is much fewer than those of the other algorithms, and it is almost a constant (averaging 12) as the signal dimension varies.

Additionally, we have designed a set of simulations to substantiate the applicability of the new method to high dimensional SAR imaging problems. To this end, we implemented the BCRA- $L_{1/2}$ -SAR method, as well as $L_{1/2}$ -SAR method, to a series of simulations. In the simulations, we fixed $s = 200$, $m = 2000$, and varied n from 2000 to 10^5 with the same interval 2000. The simulation results are then depicted in Figure 4.

It can be seen in Figure 4 (b) that the running time of BCRA- $L_{1/2}$ algorithm grows much slower than $L_{1/2}$ -SAR method as the dimension increases. More specifically, when the dimension n increases to 10^5 , the running time of the new method is 191.5 seconds, while the running time of $L_{1/2}$ -SAR method is 1591 seconds, more than 8 times of the new method. It is anticipated that more significant improvement can be obtained as the signal dimension increases. Besides, the iteration number necessary for convergence of the new method is much less than that of $L_{1/2}$ -SAR method, and it keeps very few with the order $\mathcal{O}(10)$, as shown in Figure 4 (c) and (d). Comparatively, the iteration number necessary for convergence of $L_{1/2}$ -SAR method increases faster as the signal dimension increases. Moreover, the recovery precision of the new method is much higher than $L_{1/2}$ -SAR method when the signal dimension is lower than 7.2×10^4 , as shown in Figure 4 (a). In these cases, the recovery precision of the new method is $\mathcal{O}(10^{-15})$, while those of $L_{1/2}$ -SAR method is $\mathcal{O}(10^{-5})$. However, as the signal dimension increases to 7.4×10^4 , the recovery precision of the new method gets worse sharply. This breakdown phenomenon will be further studied by the phase transition diagram in the following subsection.

3.3. Phase Transition Diagram

The phase transition diagram was firstly introduced by Donoho et al. [34] to provide a way of checking L_1/L_0 equivalence, indicating how sparsity and indeterminacy affect the success of L_1 regularization, and later it was extended as an experiment tool to study the equivalence of L_q/L_0 ($0 < q < 1$) [23] and comparing the ability of sparse reconstruction of different compressed sensing strategies [35]. We propose to apply this tool to evaluate the performance of the proposed method for SAR imaging and compare it with $L_{1/2}$ -SAR, L_1 -SAR and OMP-SAR methods. Let $\delta = m/n$ be the normalized measure of undersampling factor and $\rho = k/m$ be the normalized measure of sparsity. A plot of the pairing of variables δ and ρ describes a two-dimensional phase space $(\delta, \rho) \in [0, 1]^2$. With those notations, we implemented a series of simulation runs by taking the values of δ and ρ at 40 equispaced points in the phase space ($n = 1600$). At each point on the grid, corresponding to a SAR imaging model (2.3) with different setting of (s, m, n) (in this case $\Psi = I$ and $n = 1600$), the average of RMSE of 30 independent realizations was recorded, and a phase transition diagram of each method was then draw based on these results. The phase transition diagrams of OMP-SAR, L_1 -SAR, $L_{1/2}$ -SAR and the new methods are shown in Figure 5.

It can be seen from Figure 5 (d) that the original target scene can be reconstructed well by the new method as long as it is sufficiently sparse and enough measurements are taken. Furthermore, compared to OMP-SAR and L_1 -SAR methods, the new method uses fewer measurements to reconstruct the scene with the same sparsity, and can reconstruct much denser scene effectively when the same measurements are taken, as demonstrated by Figure 5. From another point of view, we can see that the new method has better sparse

reconstruction ability than both OMP-SAR and L_1 -SAR methods, as it demonstrates that the successful reconstruction regions (the blue regions) of Figures 5 (d) is obviously larger than those of (a) and (b). Moreover, the reconstruction ability of the new method is almost the same as $L_{1/2}$ -SAR method as shown in Figure 5 (c) and (d), which implies that the new method preserves the promoting sparsity property of $L_{1/2}$ -SAR method well. Furthermore, we calculated the percentages of the blue regions in the squares, of which the grid values are less than 0.3. The percentages of the blue regions of Figures 5 (a), (b), (c) and (d) are 41.81%, 43.56%, 53.13% and 50.25%, respectively. In terms of the percentage of the successful reconstruction region, the new method is better than both OMP-SAR and L_1 -SAR methods with more than 8% and 6% improvements, respectively, and slightly worse than $L_{1/2}$ -SAR method.

4. Applications

In this section, we demonstrate the effectiveness of the new method on real SAR data, as compared with the traditional SAR imaging method. We also compare the new method with the other three CS based SAR imaging methods aforementioned in the last section. Specifically, we employed the range doppler algorithm (RDA) [3], which is one of the most commonly used traditional SAR imaging methods. The experiment data of two real scenes were acquired from Ground-Base SAR (called GB-SAR) and RADARSAT-1, respectively. In these experiments, the algorithm settings were the same with those in simulations.

4.1. Ground-Based SAR Data Reconstruction

We have implemented the four SAR imaging methods for Ground-Based SAR data, which is acquired by the Advanced Scanning Two-dimensional Railway Observation Ground-Based SAR system of the Institute of Electronics, Chinese Academy of Sciences (called, IECAS-ASTRO Ground-Based SAR system). The interested scene composes three corner reflectors, shown as Figure 6 (a). Some related radar parameters are set as follows: the signal bandwidth is 4 GHz with carrier frequency 17 GHz, corresponding to a range resolution of 0.0375m. The pulse repetition frequency is 250 Hz, i.e., 651 pulses within dwell time $[-1.3, 1.3]$ (s) are used in this experiment. The traditional SAR reconstruction result using 651 pulses via RDA is shown in Figure 6 (b).

We applied the four sparse SAR imaging methods to the GB-SAR data by the use of different number of pulses including 651, 130 and 65. Some reconstruction results of these methods are shown in Figure 6 (the second and third rows, respectively, correspond to 130 and 65 pulses). The corresponding running times of the four sparse SAR imaging methods are listed in Table 1. As seen in Table 1, the new method is the fastest among all these methods. More specifically, the running time of the new method is no more than 11% of those of $L_{1/2}$ -SAR, L_1 -SAR and OMP-SAR methods when 651 pulses were used for reconstruction. When fewer pulses, say 130, are used to reconstruct the SAR scene, the new method is still much faster than the other sparse methods. Furthermore, when the number of pulses is reduced to 65, the running time of the new method is still much less than the other sparse methods. A remarkable feature of the new method, as compared to the other sparse SAR imaging methods, is that the running time of the new method increases much slower as the number of the measurements increases.

Additionally, as demonstrated in Figure 6 (b)-(c), there are many sidelobes and artifacts in the traditional SAR image, while the result reconstructed by the new method even only using 130 pulses is much better, that is, the new method can reconstruct the scene with higher resolution and reduced sidelobes. Especially, as compared with the other sparse SAR imaging methods, the reconstruction of the new method is better than the other three methods, since there are fewer artifacts in the reconstructions of the new method, as exhibited in Figure 6 (c) and (g). Moreover, when the number of pulses used for reconstruction is reduced to 65, both L_1 -SAR and OMP-SAR methods are failed with many artifacts in the reconstruction results, as demonstrated in Figure 6 (i) and (j). While the new method is still effective, and the reconstruction result is better than that of $L_{1/2}$ -SAR, as shown in Figure 6 (g) and (h).

4.2. RADARSAT-1 Data Reconstruction

We now show the application results of the new method for the data from RADARSAT-1 in the fine mode-2 about Vancouver region. In [2], the detailed target and data descriptions were provided. We are interested in the region of the English Bay, where there are six sitting vessels. The traditional SAR image via RDA from full sampling based on the Nyquist rate is shown in Figure 7 (a). The main radar parameters are set as follows: the signal bandwidth is 30.111 MHz, the pulse repetition frequency is 1256.98 Hz.

We applied the aforementioned four sparse SAR imaging methods to the RADARSAT-1 data with different sampling rates including 25%, 10%, 8%, and 5%. A part of the reconstruction results of these methods are shown in Figure 7. The reconstruction results with 10% and 5% sampling rates are represented in the second and third rows of Figure

7, respectively. The corresponding running times of the four SAR imaging methods are listed in Table 2. It can be seen from Table 2 that the new method is the fastest among all four methods. In particular, under the sampling rate 25%, the running time of $L_{1/2}$ -SAR, L_1 -SAR and OMP-SAR methods are about 3.5, 4 and 35 times of that of the new method. As the sampling rate descreasing, the running time of the new method is still much less than that of the other methods (less than 50% of the other methods).

Also, it can be seen that there are many sidelobes and artifacts in the traditional SAR image shown as in Figure 7 (a). As compared, the result reconstructed by the new method even with only 10% sampling is much better, with higher resolution and reduced sidelobes, as shown in Figure 7 (b). The outperformance of the new method is also supported by comparing it with the other sparsity based SAR imaging methods. Moreover, when the sampling rate is further reduced to 5%, the reconstruction of the new method is still better than the other three methods in the sense of identification and giving much clearer visual effect.

5. Conclusion

In this paper, we have suggested an accelerated $L_{1/2}$ -SAR imaging method through applying the block coordinate relaxation (BCR) technique combined with the use of reduced Newton acceleration skill. From the perspective of algorithmic implementation, the proposed method can be viewed as the following procedure: first, dividing the coordinates of unknown variables and the corresponding sensing matrix into several blocks, and then, updating all coordinate blocks sequentially via an iterative scheme. More specifically, at each iteration step, we apply $L_{1/2}$ regularization to identify the support set of each iterate

and then use the least square principle to update iterate values for each coordinate block. It is shown that the proposed method possesses the following two main advantages while preserving the sparsity and high-resolution properties of the original $L_{1/2}$ -SAR method:

(i) Fast convergence. The number of iteration for convergence is only in the order of $\mathcal{O}(10)$ in most cases, which makes it applicable to high dimensional SAR imaging applications.

(ii) High reconstruction precision. The proposed method achieves good recovery accuracy, which makes it possible to produce high quality SAR images.

The study of the present paper shows that the accelerated $L_{1/2}$ -SAR method potentially serves as an efficient SAR imaging methodology. Although we have numerically shown that the new method can converge fast within a very few iterations, the convergence property should be further justified in theory. Also, some other issues like the recovery performance bound and the minimal number of measurements should be further investigated. Furthermore, how to fast implement the new method through the way of parallel computing, or other high performance computing (HPC) techniques, such as Graphic Processing Unit (GPU) technique, should be further studied.

- [1] J. C. Curlander, R. N. McDonough, Synthetic Aperture Radar: Systems and Signal Processing, New York: Wiley, 1991.
- [2] I. G. Cumming, F. H. Wong, Digital processing of synthetic aperture radar data: algorithms and implementation, Artech House Publishers Press, 2004.
- [3] C. Wu, A digital system to produce imagery from SAR data, AIAA Conference: System Design Driven by Sensors, 1976.

- [4] A. Moreira, J. Mittermayer, R. Scheiber, Extended chirp scaling algorithm for air- and spaceborne SAR data processing in stripmap and ScanSAR imaging modes, *IEEE Transaction on Geoscience and Remote Sensing*, 34 (1996), 1123-1136.
- [5] J.H.G. Ender, On compressive sensing applied to radar, *Signal Processing*, 90 (2010), 1402-1414.
- [6] R. Baraniuk, P. Steeghs, Compressive radar imaging, *IEEE Radar Conference*, Waltham, MA, (2007), 128-133.
- [7] M. Alonso, P. Lopez-Dekker, J. J. Mallorqui, A novel strategy for radar imaging based on compressive sensing, *IEEE Trans. on Geoscience and Remote Sensing*, 48 (2010), 4285-4295.
- [8] V. Patel, G. Easley, D. Hearnly, R. Chellappa, Compressed synthetic aperture radar, *IEEE Journal of Selected Topics in Signal Processing*, 4 (2010), 244-254.
- [9] L. C. Potter, E. Ertin, J. T. Parker, M. Cetin, Sparsity and compressed sensing in radar Imaging, In *Proceedings of the IEEE*, 98 (2010), 1006-1020.
- [10] J. S. Zeng, Z. B. Xu, H. Jiang, B. C. Zhang, W. Hong, Y. R. Wu, SAR imaging from compressed measurements based on $L_{1/2}$ regularization, *IEEE International Geoscience and Remote Sensing Symposium (IGARSS)*, Vancouver, (2011), 625-628.
- [11] J. S. Zeng, J. Fang, Z. B. Xu, Sparse SAR imaging based on $L_{1/2}$ regularization, *Science in China Series F-Information Science*, 55 (2012), 1755-1775.

- [12] E. J. Candes, J. Romberg, T. Tao, Robust uncertainty principles: exact signal reconstruction from highly incomplete frequency information, *IEEE Trans. on Information Theory*, 52 (2006), 489-509.
- [13] D. L. Donoho, Compressed sensing, *IEEE Trans. on Information Theory*, 52 (2006), 1289-1306.
- [14] J. A. Tropp, A. Gilbert, Signal recovery from random measurements via orthogonal matching pursuit, *IEEE Trans. on Information Theory*, 53 (2007), 4655-4666.
- [15] D. Needell, R. Vershynin, Signal recovery from incomplete and inaccurate measurements via Regularized Orthogonal Matching Pursuit, *IEEE Journal of Selected Topics in Signal Processing*, 4 (2010), 310-316.
- [16] J. A. Tropp, S. Wright, Computational methods for sparse solution of linear inverse problems, In *Proceedings of the IEEE*, 98 (2010), 948-958.
- [17] I. Duabeachies, M. Defrise, C. Mol, An iterative thresholding algorithm for linear inverse problems with a sparse constraint, *Communications on Pure and Applied Mathematics*, 57 (2004), 1413-1457.
- [18] A. Beck, M. Teboulle, A fast iterative shrinkage-thresholding algorithm for linear inverse problems, *SIAM J. imaging sciences*, 2 (2009), 183-202.
- [19] E. van den Berg and M. P. Friedlander, SPGL1: A solver for large-scale sparse reconstruction, *[http : //www.cs.ubc.ca/labs/scl/spgl1](http://www.cs.ubc.ca/labs/scl/spgl1)*.

- [20] E. T. Hale, W. Yin, Y. Zhang, Fixed-point continuation for l_1 -minimization: methodology and convergence, SIAM Journal on Optimization, 19 (2008), 1107-1130.
- [21] D. L. Donoho, High-dimensional centrally symmetric polytopes with neighborliness proportional to dimension, Discrete and Comput. Geom., 35 (2006), 617-652.
- [22] Z. B. Xu, H. Zhang, Y. Wang, X. Y. Chang, Y. Liang, $L_{\frac{1}{2}}$ regularizer, Science in China Series F-Information Science, 53 (2010), 1159-1169.
- [23] Z. B. Xu, H. L. Guo, Y. Wang, H. Zhang, The Representation of $L_{1/2}$ regularizer among $L_q(0 < q < 1)$ regularizer: an experimental study based on phase diagram, Acta Automatic Sinica, 38 (2012), 1225-1228.
- [24] Z. B. Xu, X. Y. Chang, F. M. Xu, H. Zhang, $L_{1/2}$ Regularization: a thresholding representation theory and a fast solver, IEEE Trans. on Neural Networks and Learning Systems, 23 (2012), 1013-1027.
- [25] R. Chartrand, V. Staneva, Restricted isometry properties and nonconvex compressive sensing, Inverse Problems, 24 (2008), 1-14.
- [26] E. Polak, Computational methods in optimization: a unified approach, Academic Press, New York, NY, 1971.
- [27] S. Sardy, A. Bruce, P. Tseng, Block coordinate relaxation methods for nonparametric wavelet denoising, Journal of Computational and Graphical Statistics, 9 (2000), 361-379.

- [28] Z. Q. Luo, P. Tseng, On the convergence of the coordinate descent method for convex differential minimization, *Journal of Optimization Theory and Applications*, 72 (1992), 7-35.
- [29] P. Tseng, Convergence of a block coordinate descent method for nondifferential minimization, *Journal of Optimization Theory and Applications*, 109 (2001), 475-494.
- [30] Stephen J. Wright, Accelerated block-coordinate relaxation for regularized optimization, [http : //www.optimization – online.org/DB_HTML/2010/08/2702.pdf](http://www.optimization-online.org/DB_HTML/2010/08/2702.pdf).
- [31] B. Efron, R. Tibshirani, Improvements on cross-validation: the .632+ bootstrap method, *Journal of the American Statistical Association*, 92 (1997), 548-560.
- [32] G. H. Golub, M. Heath, G. Wahba, Generalized cross-validation as a method for choosing a good ridge parameter, *Technometrics*, 21 (1979), 215-223.
- [33] T. Blumensath, M. E. Davies, Iterative hard thresholding for compressed sensing, *Applied and Computational Harmonic Analysis*, 27 (2009), 265-274.
- [34] D. L. Donoho, J. Tanner, Observed universality of phase transitions in high-dimensional geometry, with applications in modern signal processing and data analysis. *Philos Trans Royal Soc A*, 367(2009), 4273–4293.
- [35] H. Zhang, Y. Liang, H. L. Guo, Z.B. Xu. The essential ability of sparse reconstruction of different compressive sensing strategies. *Sci China Inf Sci*, 2011, doi:10.1007/s11432-011-4502-6.

Algorithm1 : BCRA- $L_{1/2}$ Algorithm

Input : The measurement matrix Φ and measurements y .

Block Partition : Partition the coordinates of unknown variable $x \in \mathbb{C}^n$ and the columns of Φ into $|Q|$ blocks without intersection, say, $\{x_{[q]}|q \in Q\}$ and $\{\Phi_{[q]}|q \in Q\}$, where $Q = \{1, 2, \dots, |Q|\}$ is the index set of blocks, and $x_{[q]}$, $\Phi_{[q]}$ are the coordinates of x and Φ corresponding to index set $[q]$. Given step-sizes $\{\mu_q|q \in Q\}$.

Initialization : Initialize $x^{(0)} = 0$, let $k := 0$.

Step 1: Calculate: $\Phi_{[q]}x_{[q]}^{(k)}$, $q = 1, 2, \dots, |Q|$, and $r^{(k)} = y - \sum_{q=1}^{|Q|} \Phi_{[q]}x_{[q]}^{(k)}$;

Step 2: Update regularization parameter $\lambda^{(k)}$;

Step 3: Update all blocks sequentially at $k + 1$ -th iteration

for $q = 1 : |Q|$

(1) Calculate $y_q^{(k)} = r^{(k)} + \Phi_{[q]}x_{[q]}^{(k)}$, $B_{\mu_q}(x_{[q]}^{(k)}) = x_{[q]}^{(k)} + \mu_q \Phi_{[q]}^H(y_q^{(k)} - \Phi_{[q]}x_{[q]}^{(k)})$;

(2) (Form Signal Proxy) Update $\hat{x}_{[q]}^{(k+1)}$ via iterative half thresholding scheme:

$$\hat{x}_{[q]}^{(k+1)} = H_{\lambda^{(k)}\mu_q, 1/2}(B_{\mu_q}(x_{[q]}^{(k)})),$$

(3) (Identify Support Set) Identify $S_{[q]}^{(k+1)}$:

$$S_{[q]}^{(k+1)} = \text{supp}(\hat{x}_{[q]}^{(k+1)}), P_{[q]} = I_{|[q]|}|_{S_{[q]}^{(k+1)}}, \Phi_{S,q} = P_{[q]}\Phi_{[q]};$$

(4) (Signal Estimation) Estimate the q -th block coordinates $x_{[q]}^{(k+1)}$:

$$x_s^{(k+1)} = \arg \min_{x_s \in \mathbb{C}^{|S_{[q]}^{(k+1)}|}} \left\{ \|y_q^{(k)} - \Phi_{S,q}x_s\|_2^2 \right\}, x_{[q]}^{(k+1)} = P_{[q]}x_s^{(k+1)};$$

end for

Step 4. Termination check: if yes, then the iteration stops; otherwise, let $k := k + 1$,

return to **Step 1**.

Output : $x^{(k+1)}$.

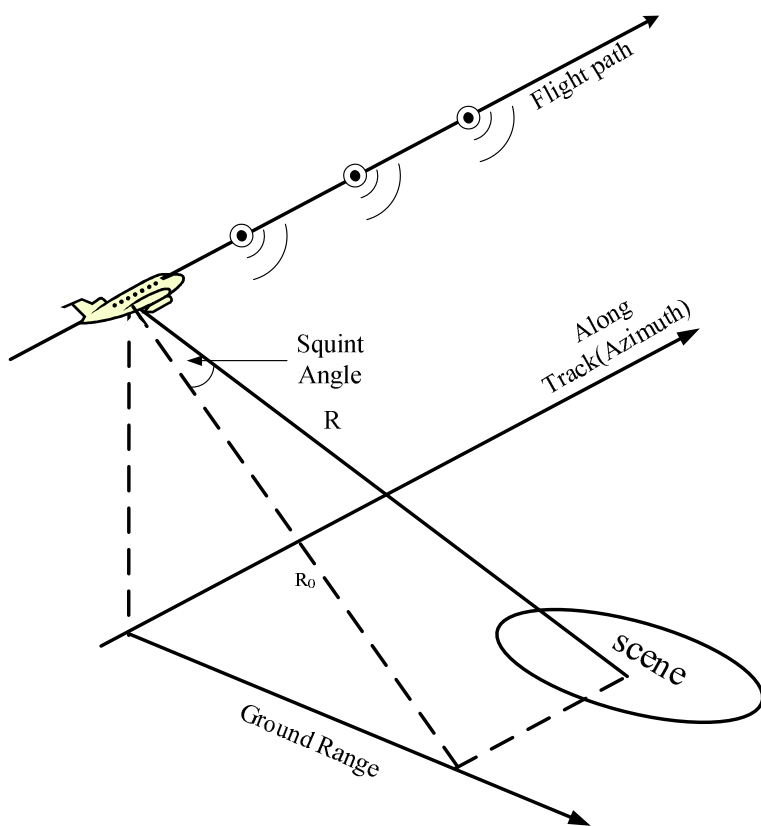


Figure 1: SAR data acquisition geometry of stripmap-mode SAR.

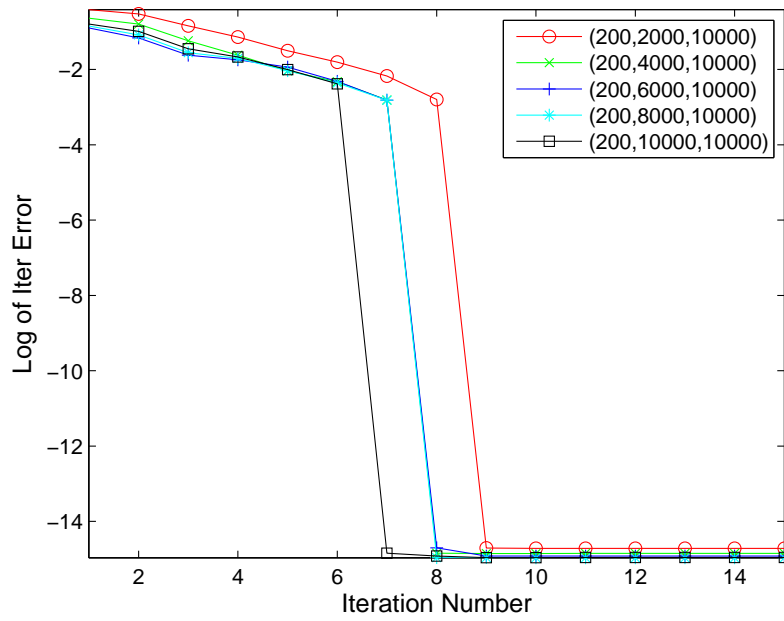
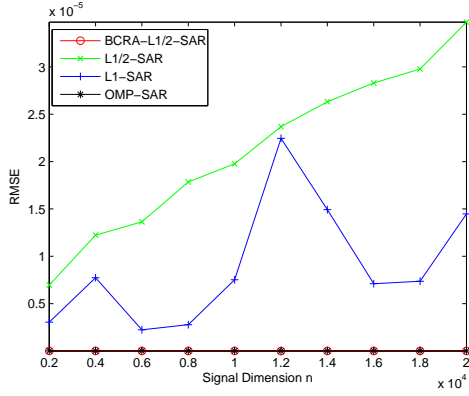
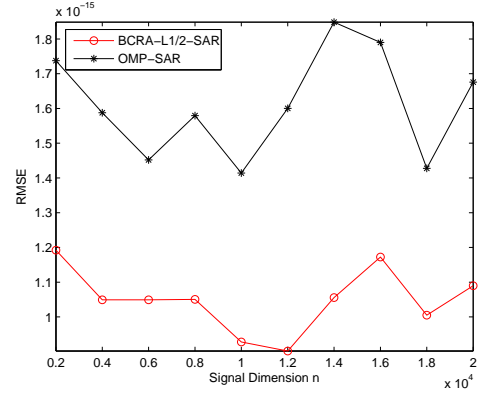


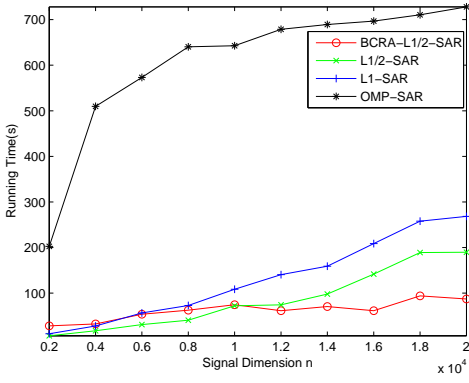
Figure 2: Fast convergence of BCRA- $L_{1/2}$ algorithm with different measurements. The horizontal axis represents the iteration number, and the vertical axis represents the iterative error in the logarithmic scale with 10 as the base.



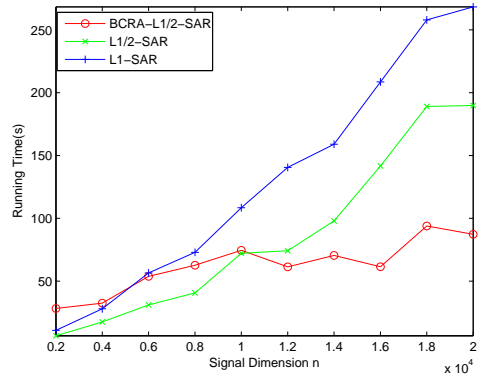
(a) RMSE



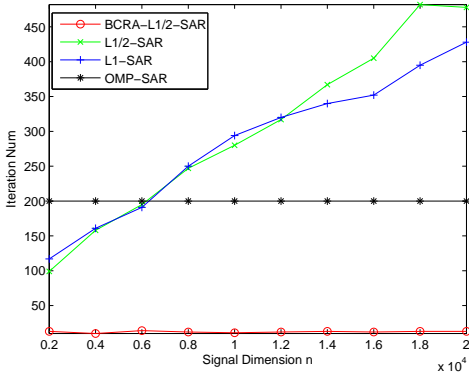
(b) Detailed RMSE



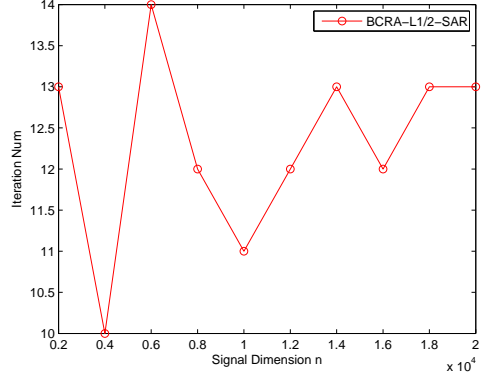
(c) Running time (RT)



(d) Detailed RT

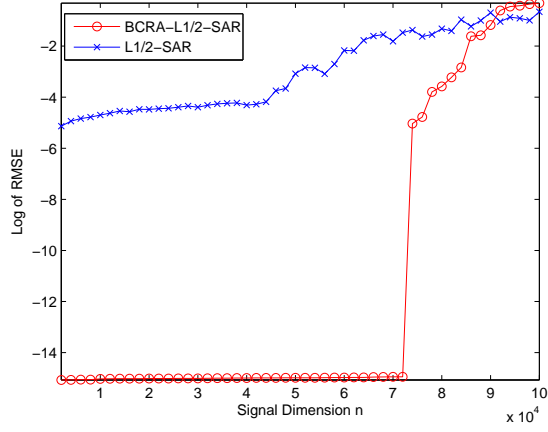


(e) Iteration Number (IterN)

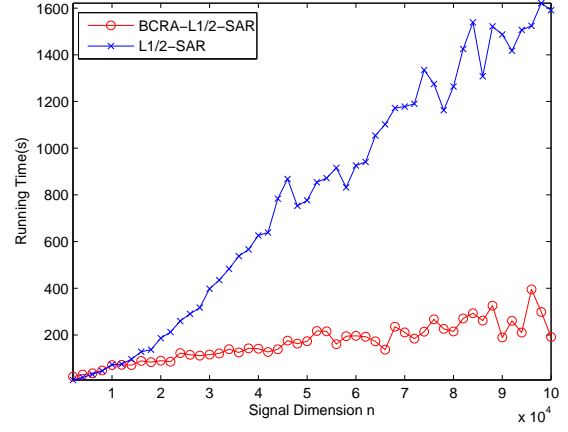


(f) IterN of BCRA- $L_{1/2}$

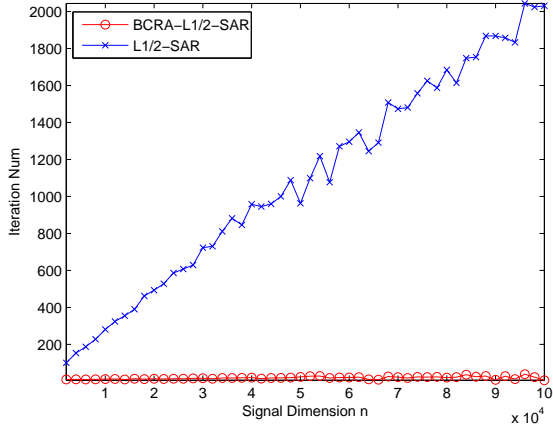
Figure 3: Simulations with different signal dimensions. (a) The tendency curve of RMSE with different dimensions varying from 2000 to 20000. (b) Detailed comparison on RMSE of BCRA- $L_{1/2}$ and OMP. (c) The tendency curve of the running time (RT) for different algorithms. (d) Detailed comparison on RT. (e) The tendency curve of the iteration number (IterN) necessary for different algorithms. (f) IterN necessary for BCRA- $L_{1/2}$.



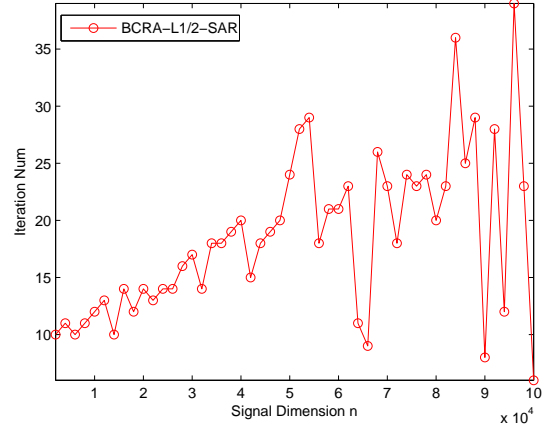
(a) Comparison on RMSE



(b) Comparison on RT

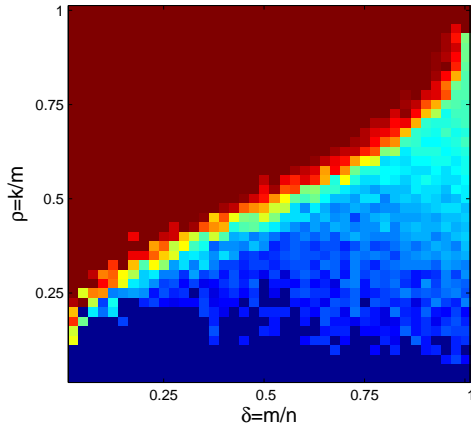


(c) Comparison on IterN

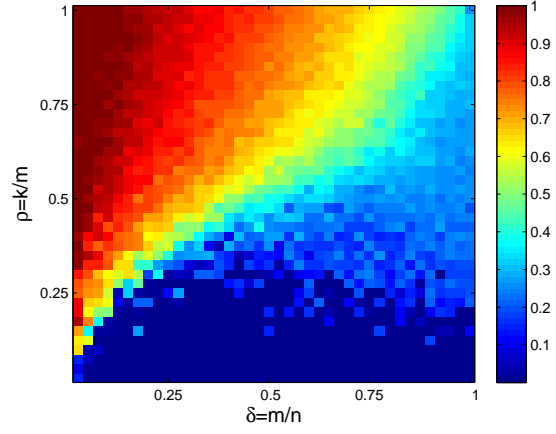


(d) IterN of BCRA- $L_{1/2}$

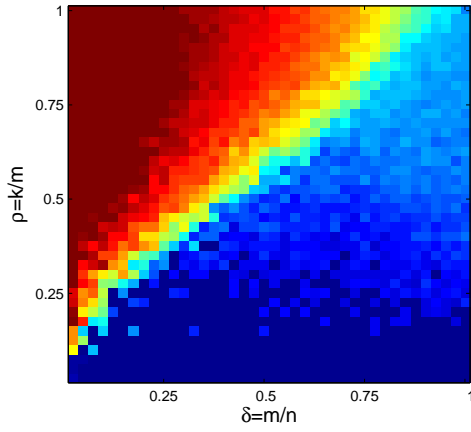
Figure 4: Comparison for applicability to high dimensional SAR imaging problems. (a) Comparison on tendency of RMSE in the logarithmic scale with 10 as the base. (b) Comparison on tendency of the running time. (c) Comparison on tendency of the iteration number. (d) The tendency of the iteration number necessary for BCRA- $L_{1/2}$.



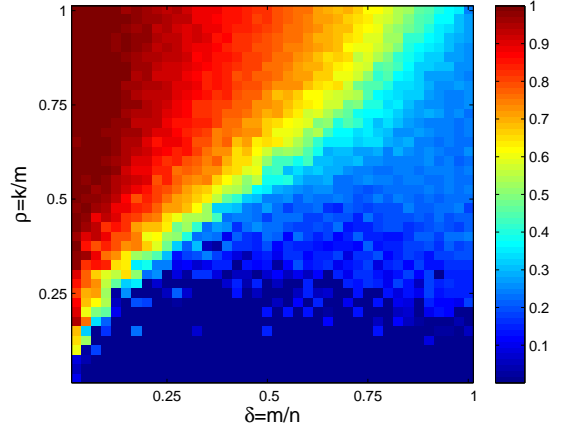
(a) OMP-SAR



(b) L_1 -SAR



(c) $L_{1/2}$ -SAR



(d) BCRA- $L_{1/2}$ -SAR

Figure 5: The phase transition diagrams of OMP-SAR, L_1 -SAR, $L_{1/2}$ -SAR and BCRA- $L_{1/2}$ -SAR methods when applied to SAR imaging. (a) OMP-SAR method; (b) L_1 -SAR method; (c) $L_{1/2}$ -SAR method; (d) BCRA- $L_{1/2}$ -SAR method.

Pulses	BCRA- $L_{1/2}$ -SAR	$L_{1/2}$ -SAR	L_1 -SAR	OMP-SAR
651	8.22	79.25	79.22	138.95
130	4.31	8.48	8.95	21.0156
65	3.64	5.70	5.45	12.47

Table 1: The running time for GB-SAR data (unit: second)

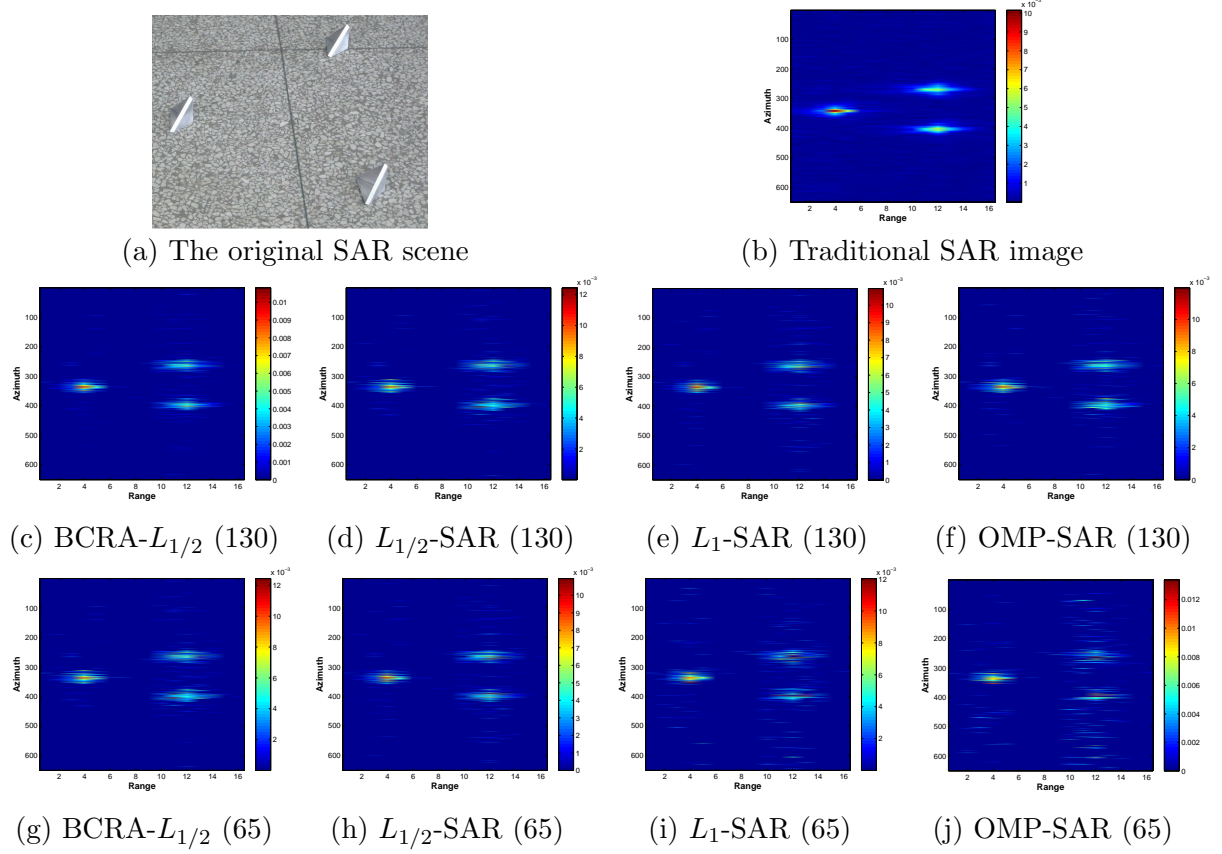
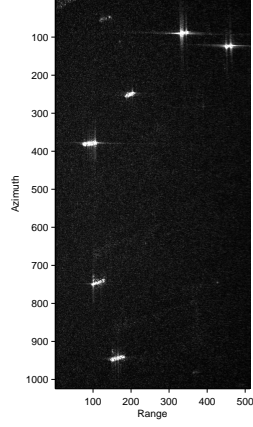


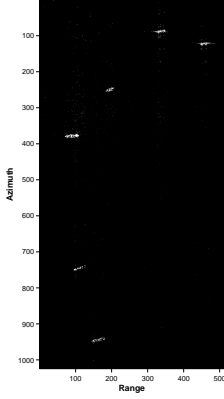
Figure 6: Reconstruction results of Ground-Based SAR data via different SAR imaging methods using different pulses. (a) The original SAR scene with three corner reflectors. (b) The traditional SAR reconstruction via RDA using 651 pulses, which is sampled at the traditional Nyquist rate. (c), (d), (e) and (f) represent the reconstruction results of BCRA- $L_{1/2}$ -SAR, $L_{1/2}$ -SAR, L_1 -SAR, and OMP-SAR methods using 130 pulses, respectively. (g), (h), (i) and (j) are the reconstruction results of BCRA- $L_{1/2}$ -SAR, $L_{1/2}$ -SAR, L_1 -SAR, and OMP-SAR methods using 65 pulses, respectively.

Sampling Rate(%)	BCRA- $L_{1/2}$ -SAR	$L_{1/2}$ -SAR	L_1 -SAR	OMP-SAR
25	363.60	1240.22	1454.80	12403.20
10	214.68	511.63	663.45	5273.64
8	198.88	454.98	534.58	3578.59
5	152.28	330.55	377.39	1578.59

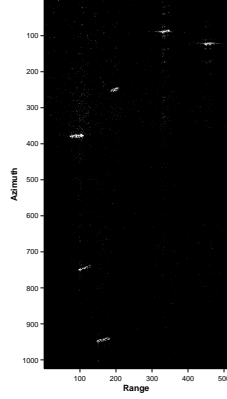
Table 2: The running time for RADARSAT-1 data (unit: second)



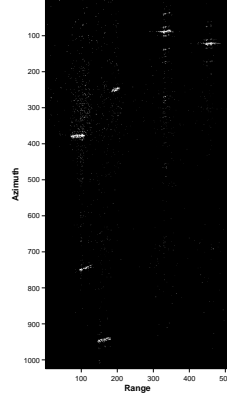
(a) Traditional SAR image



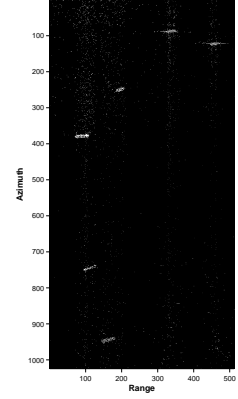
(b) BCRA- $L_{1/2}$ (10%)



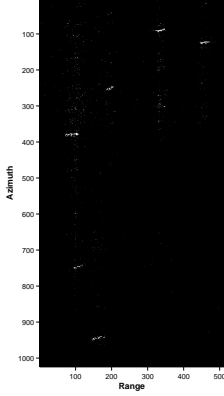
(c) $L_{1/2}$ -SAR (10%)



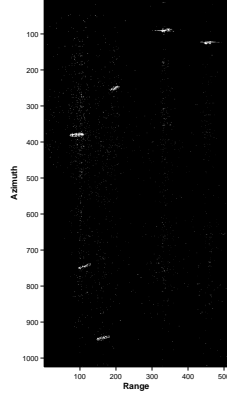
(d) $L_{1/2}$ -SAR (10%)



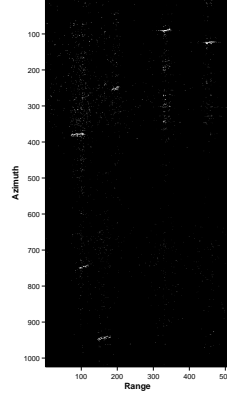
(e) OMP-SAR (10%)



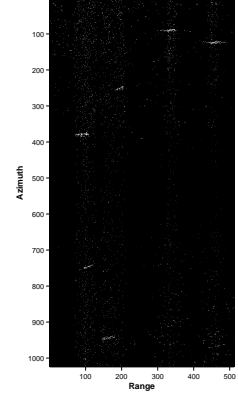
(f) BCRA- $L_{1/2}$ (5%)



(g) $L_{1/2}$ -SAR (5%)



(h) L_1 -SAR (5%)



(i) OMP-SAR (5%)

Figure 7: Reconstruction results of RADARSAT-1 SAR data via different SAR imaging methods with different sampling rates. (a) Traditional SAR image via RDA with full sampling based on the Nyquist rate. (b)-(i) represent the reconstruction results of BCRA- $L_{1/2}$ -SAR, $L_{1/2}$ -SAR, L_1 -SAR and OMP-SAR methods with 10% and 5% sampling rates, respectively.